SCIENTIFIC REPORTS

OPEN

SUBJECT AREAS:
PEPTIDES
SODIUM CHANNELS

Received
14 August 2014

Accepted
18 February 2015

Published
18 March 2015

Synergetic Action of Domain II and IV Underlies Persistent Current Generation in $Na_v1.3$ as revealed by a tarantula toxin

Cheng Tang[1]*, Xi Zhou[1]*, Yunxiao Zhang[1], Zhaohua xiao[2], Zhaotun Hu[1], Changxin Zhang[1], Ying Huang[1], Bo Chen[1], Zhonghua Liu[1] & Songping Liang[1]

[1]College of Life Science, Hunan Normal University, Changsha, Hunan, 410081, China, [2]Department of Pediatrics, Xiangya Hospital of Central South University, Changsha, Hunan, 410008, China.

Correspondence and requests for materials should be addressed to Z.L. (liuzh@hunnu.edu.cn) or S.L. (liangsp@hunnu.edu.cn)

* These authors contributed equally to this work.

The persistent current (I_{NaP}) through voltage-gated sodium channels enhances neuronal excitability by causing prolonged depolarization of membranes. $Na_v1.3$ intrinsically generates a small I_{NaP}, although the mechanism underlying its generation remains unclear. In this study, the involvement of the four domains of $Na_v1.3$ in I_{NaP} generation was investigated using the tarantula toxin α-hexatoxin-MrVII (RTX-VII). RTX-VII activated $Na_v1.3$ and induced a large I_{NaP}. A pre-activated state binding model was proposed to explain the kinetics of toxin-channel interaction. Of the four domains of $Na_v1.3$, both domain II and IV might play important roles in the toxin-induced I_{NaP}. Domain IV constructed the binding site for RTX-VII, while domain II might not participate in interacting with RTX-VII but could determine the efficacy of RTX-VII. Our results based on the use of RTX-VII as a probe suggest that domain II and IV cooperatively contribute to the generation of I_{NaP} in $Na_v1.3$.

Voltage-gated sodium channels (Na_vs) are essential for the initiation and propagation of action potentials in excitable tissues such as nerves and muscles[1–3]. They consist of a pore forming α-subunit (260 kDa) associated with auxiliary β-subunits (30–40 kDa)[4]. In mammals, nine α-subtypes ($Na_v1.1$–1.9) have been identified and cloned[5,6]. The α-subunit is composed of four homologous domains (DI–DIV) and each domain contains six transmembrane segments (S1–S6). The S5–S6 segments form a central pore for Na^+, with the S1–S4 segments from each domain forming the surrounding voltage sensors[2,4]. Each of the four voltage sensors is activated in response to depolarization of membrane potential[7]; the voltage sensors of the first three domains (DI–III) are responsible for channel activation, while that of the fourth domain (DIV) determined fast inactivation[8,9]. Na_vs fail to inactivate in some cases, resulting in the generation of non-inactivating persistent Na^+ currents (I_{NaP}), which account for up to 5% of the transient peak inward current (I_{NaT}) in physiological conditions[10,11]. Despite its small amplitude compared with I_{NaT}, I_{NaP} amplifies synaptic potentials and aids in the repetitive firing of action potentials (AP) in neurons because it is activated by sub-threshold voltages[11]. The voltage range in which I_{NaP} is activated is traversed by interspike intervals during an AP train[11,12]. I_{NaP} has been characterized in a variety of neurons[13]. Mutations in some Na_vs genes causing enhanced I_{NaP} amplitude are correlated to diseases, such as heart vascular disease and epilepsy[11,14,15]. Therefore, drugs targeting I_{NaP} are expected to have therapeutic benefits[16–18].

The early understanding of the origin of I_{NaP} is based on three hypotheses: (1) the window current hypothesis[19]; (2) I_{NaP} is generated by unusual subtypes of Na_vs which lacking inactivation[20,21]; (3) I_{NaP} is produced by the same population of channels responsible for I_{NaT} through a distinct gating mechanism[22,23]. Many lines of evidences support the third hypothesis, namely that some channels of a specific Na_v subtype occasionally enter the late brief opening and burst of opening state in single channel recordings[24–26]. The single channel mechanism for the slowed inactivation of a Na_v by site 3 toxins TsIV-5 and anthopleurin B was also attributed to the increment of mean open time as well as prolonged bursting[27,28]; studies showed that mutations in all four domains of Na_vs as well as intracellular loops affect the amplitude of the I_{NaP}[29]; wild type (wt)-$Na_v1.3$ naturally develops I_{NaP} in neonatal and axotomized neurons[30,31], and $Na_v1.3$ expressed in HEK293T cells displays a clearly detectable I_{NaP}[32,33]. These data

also confirm that I_{NaP} is the intrinsic property of Na_vs themselves, although the molecular determinants of I_{NaP} in Na_vs are largely unknown.

In the present study, we identified a tarantula toxin named α-hexatoxin-MrVII (RTX-VII) that enhances the I_{NaP} of $Na_v1.3$ and used it as a probe to examine the involvement of each domain of $Na_v1.3$ in the generation of I_{NaP}. Our results reveal that domains II and IV work in a synergetic manner to determine the toxin-induced I_{NaP} of $Na_v1.3$.

Results

RTX-VII enhances the I_{NaP} of $Na_v1.3$. *Macrothele raveni* (Figure 1a, *inset*) venom was collected by using an electro-pulse stimulator as described previously[34]. The lyophilized crude venom was fractionated by RP-HPLC (Figure 1a). A comprehensive screening of each eluted fraction against $Na_v1.3$ transiently expressed in HEK293T cells indicated that the fraction with a retention time of 44.6 min inhibited the fast inactivation of this channel (Figure 1b). This fraction contained a peptide with a molecular weight of 4064.71 Da as determined by MALDI-TOF MS, which was then further purified by analytical RP-HPLC (Supplementary Fig. S1a). Sequence of the peptide was determined by combining Edman degradation (Supplementary Fig. S1j) and cDNA sequencing (Supplementary Fig. S1b), and the toxin was named α-hexatoxin-MrVII (RTX-VII). Blasting the full amino acid sequence of RTX-VII showed that it share 92% identity to a previously known spider toxin Magi-6 (Supplementary Fig. S1c). However, Magi-6 did not compete with the scorpion toxin LqhαIT in binding site 3 of Na_vs, and the symptoms caused by injection of pure Magi-6 to mice could not be directly linked to a particular ion channel receptor[35]. This raise the possibility that the subtle amino acid sequence variation brought by RTX-VII makes it active on mammalian Na_vs, as that of APETx3 and APETx1, in which a single amino acid substitution between them confer these two toxins different ion channel selectivity[36]. RTX-VII contains eight cysteine residues forming four disulfide bonds, as the measured molecular weight was 8 Da less than the theoretical one. The conserved arrangement of the cysteine residues in RTX-VII indicated that it contains a cystine knot (ICK) motif (Supplementary Fig. S1c).

As shown in Figure 1b, RTX-VII had three effects on current of $Na_v1.3$: (1) it increased the I_{NaT} amplitude at the depolarizing voltage of −10 mV; (2) it inhibited the fast inactivation of the channel as determined by I_{5ms}/I_{NaT} ratio; (3) and it induced a large I_{NaP} as revealed by the I_{45ms}/I_{NaT} ratio. At a depolarization of −10 mV, the I_{NaP} generated by $Na_v1.3$ accounted for little of the I_{NaT} under control conditions, whereas the treatment with 0.1 μM RTX-VII enhanced the I_{NaP} to approximate 25% of the I_{NaT}. The I_{NaP} evoked by the toxin lasted for several seconds and large tail current was

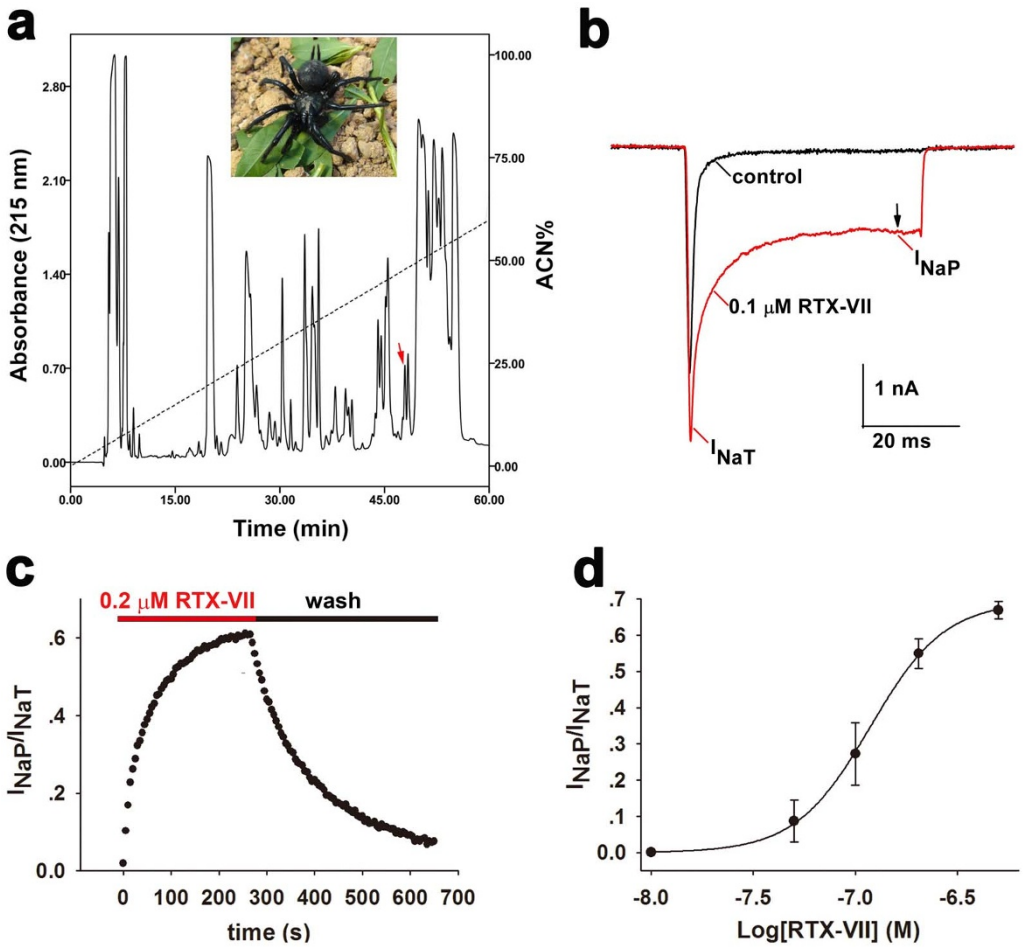

Figure 1 | RTX-VII induces large I_{NaP} in $Na_v1.3$. (a) RP-HPLC profile of the venom from the spider *Macrothele raveni* (*inset, photo by Dr Songping Liang*), where red arrow indicates the fraction containing RTX-VII. (b) Current traces from a representative cell show 0.1 μM RTX-VII enhances the I_{NaT} of $Na_v1.3$ and induces a large I_{NaP} at the end of a 50-ms depolarization to −10 mV from a holding potential of −100 mV (n = 6). Note I_{NaP} was measured at the time point of 45 ms. (c) Time course for the enhancement of I_{NaP} of $Na_v1.3$ by 0.2 μM RTX-VII and the recovery upon washing with bath solution, τ_{on} and τ_{off} is 40.9 ± 11.3 s and 162.8 ± 39.7 s, respectively (n = 4). (d) RTX-VII dose dependently enhances I_{NaP} of $Na_v1.3$ with an apparent EC_{50} of 0.12 μM (n = 6). The maximum response (f_{max}) and the minimum response (f_{min}) of $Na_v1.3$ to RTX-VII is 66.90% and 0, respectively.

observed when cell membrane was repolarized (Supplementary Fig. S1d), distinguishing this toxin from certain α-scorpion toxins. The time course for 0.2 μM RTX-VII activating the I_{NaP} of $Na_v1.3$ was characterized by a slow onset of action (τ_{on} = 40.9 ± 11.3 s) and a slow recovery upon washing (τ_{off} = 162.8 ± 39.7 s) (Figure 1c). The activation of the I_{NaP} of $Na_v1.3$ by RTV-VII was dose-dependent, with an apparent EC_{50} of 120 nM (Figure 1d). The activity and selectivity of RTX-VII were examined against three Na_v subtypes ($Na_v1.4$, 1.5 and 1.7) expressed in HEK293T cells, TTX-R Na_vs of rat dorsal root ganglion neurons and Na_vs in neonatal rat hippocampal neurons. Among these channels, Na_vs of neonatal rat hippocampal neurons were sensitive to this toxin (Supplementary Fig. S1i), whereas the others were not (Supplementary Fig. S1e–h).

Kinetics of RTX-VII action on $Na_v1.3$. The current-voltage (I–V) relationships of the I_{NaT} and I_{NaP} of $Na_v1.3$ before and after the application of 0.2 μM RTX-VII were explored (Figure 2, Supplementary Fig. S2). Compared with the control, RTX-VII modified the I–V relationship of the I_{NaT} as follows: (1) the activation of the I_{NaT} was potentiated by the toxin at voltages ranging from −45 mV to 10 mV, while no potentiation was observed at voltages > 10 mV (Figure 2a); (2) the activation voltage of the maximum I_{NaT} was shifted from 5 mV in the control to −10 mV in the presence of the toxin (Figure 2a, Supplementary Fig. S2d). Although RTX-VII did not alter the reversal voltages (approximate 65 mV) of $Na_v1.3$, toxin application did negatively shift channels' initial activation voltage (Figure 2a and c). These data indicate that the toxin treatment may increase the opening probability of $Na_v1.3$ channels in cell membrane and facilitate their activation at weak depolarizing voltages. The I–V curves of the I_{NaP} before and after the application of toxin indicate that the enhancement of the I_{NaP} by the toxin occurred across the depolarizing voltages tested (Figure 2a, Supplementary Fig. S2a) and the activation voltage of the maximum I_{NaP} was at about −10 mV. Regarding the I–V curves of the I_{NaP} and I_{NaT} in the presence of toxin, if the amplitudes of the I_{NaP} and I_{NaT} at each depolarizing voltage were normalized to their maximum one, respectively, they overlapped completely (Figure 2b), suggesting that the I_{NaP} and I_{NaT} in the presence of the toxin share rather similar activation voltage. Similar to some α-scorpion toxins[37], RTX-VII removed the fast inactivation of $Na_v1.3$ in a voltage-independent way at depolarizing voltages ranging from −20 mV to +30 mV (Supplementary Fig S2b).

The conductance-voltage (G–V) relationship and the steady-state inactivation of $Na_v1.3$ before and after the application of RTX-VII were explored (Figure 2d). Compared with the control, RTX-VII increased the conductance of the cell membrane at depolarizing voltages below 10 mV as revealed by an approximate 16 mV negative shift of $Na_v1.3$ channels' activation curve induced by the toxin (V_a = −12.72 ± 4.92 mV for control and V_a = −29.64 ± 6.21 mV for the toxin treatment), which is in accordance with the negative shift of the activation voltage for maximum I_{NaT} observed in the I–V curve; the toxin did not significantly alter the slope factor of the activation curve (K_a = 6.83 ± 0.98 mV for control and K_a = 5.66 ± 1.12 mV for the toxin treatment). The I–V and G–V relationships

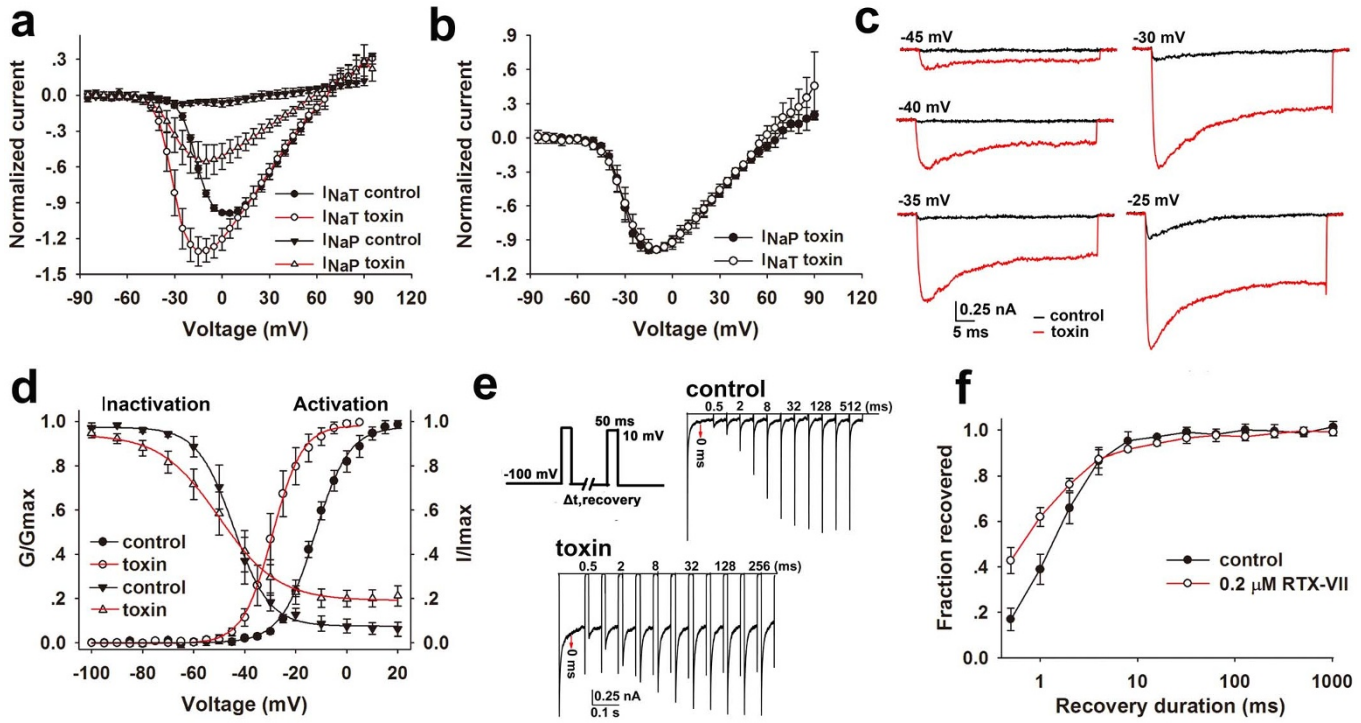

Figure 2 | Kinetics for RTX-VII interacting with $Na_v1.3$. (a) I–V curves of the I_{NaP} and I_{NaT} of $Na_v1.3$ before and after 0.2 μM RTX-VII treatment. Each current component was normalized to the maximum I_{NaT} in control (n = 11). (b) I-V curves of the I_{NaT} and I_{NaP} of $Na_v1.3$ in the presence of 0.2 μM RTX-VII. The I_{NaP} and I_{NaT} at each depolarizing voltage were normalized to their maximum one, respectively (n = 11). (c) A cluster of current traces from a representative cell show that 0.2 μM RTX-VII enhances the I_{NaT} and I_{NaP} of $Na_v1.3$ at various depolarizing voltages (n = 11). (d) 0.2 μM RTX-VII causes a hyperpolarized shift of the steady-state activation curve of $Na_v1.3$ without changing the slope factor (V_a = −12.72 ± 4.92 mV for control and V_a = −29.64 ± 6.21 mV for the toxin treatment; K_a = 6.83 ± 0.98 mV for control and K_a = 5.66 ± 1.12 mV for the toxin treatment) (n = 11), as well as a small but significant hyperpolarized shift of the steady-state inactivation accompanied by a significant change of the slope factor (V_h = −44.58 ± 2.73 mV for control and V_h = −51.12 ± 5.00 for the toxin treatment, $p < 0.05$; K_a = −6.98 ± 1.44 mV for control and K_a = −12.49 ± 0.41 mV for the toxin treatment, $p < 0.001$) (n = 5). (e) Representative traces shows the recovery of $Na_v1.3$ from fast inactivation before (*control*) and after (*toxin*) 0.2 μM RTX-VII treatment. The red arrow indicates the recovery duration of 0 ms; the numbers labeled above the traces show the recovery time. The repriming protocol is also shown (n = 5). (f) Time-dependent recovery of $Na_v1.3$ from fast inactivation in the presence and absence of 0.2 μM RTX-VII (n = 5).

of $Na_v1.3$ before and after RTX-VII application were acquired with stringent controls of the uncompensated series resistance (Rs) caused depolarizing voltage error (the maximum tolerable voltage error was less than 5 mV, the mean maximum Rs-caused voltage error was 2.34 ± 1.08 mV, $p < 0.001$ when compared to the *Va* shifted amplitude). A steady-state component (approximate 20% of the I_{NaT}) that was resistant to inactivation was observed in the steady-state inactivation (SSI) curve when conditional voltages were above −20 mV, which should represent the I_{NaP} elicited by conditional pulses. A significant change of V_h and K_h were observed ($V_h = -44.58 \pm 2.73$ mV for control and $V_h = -51.12 \pm 5.00$ mV for the toxin treatment, $p < 0.05$; $K_h = -6.98 \pm 1.44$ mV for control and $K_h = -12.49 \pm 0.41$ mV for the toxin treatment, $p < 0.001$). The hyperpolarization shift of the G–V curve and a non-inactivated component in the SSI curve together resulted in an enlarged voltage range for generation of window current, indicating a slower development of closed state inactivation (CSI) in the toxin-treated channels.

The effect of RTX-VII on the repriming kinetics (recovery from fast inactivation) of $Na_v1.3$ was also investigated. As shown in Figure 2e, the I_{NaT} of $Na_v1.3$ recovered gradually from fast inactivation with the repolarizing time (recovery time) increasing in the absence (*control*) and presence (*toxin*) of RTX-VII. The I_{NaP} induced by the toxin was observed at all recovery time. The I_{NaP} of the toxin-treated channels fully recovered at the recovery time of 0 ms, but no I_{NaT} recovery was observed (Figure 2e, *toxin*). The recovery ratios of $Na_v1.3$ I_{NaT} before and after the application of toxin were plotted as a function of recovery time (Figure 2f), showing most of channels (>80%) recovered from fast inactivation in 4 ms in both conditions. An apparently faster repriming of the toxin-treated channels than that of control channels within 4 ms was observed, which could be associated with the existence of the I_{NaP}. If the I_{NaP} was subtracted from the I_{NaT} in toxin treated channels, the residual current would exhibit the same repriming kinetics as that of the control (Supplementary Fig. S2c).

The molecular mechanism of RTX-VII as an excitatory toxin. The enhancement of I_{NaP} of Na_vs in hippocampal neurons by RTX-VII may have led to excitatory toxic in mouse. Intracerebroventricular injection of 20 ng RTX-VII dissolved in 20 μl saline caused seizure-like symptoms, as described by circular running in the first several minutes followed by involuntary body twitching, while animals in control group injected with 20 μl saline behaves normal ($n = 5$ in each group, Supplementary video). We therefore investigated the mechanism of RTX-VII as excitatory toxin. $Na_v1.3$ is upregulated in the peripheral nervous system in response to nerve injury, and contributes to the hyperexcitability of nociceptive neurons under neuropathic conditions[38,39]. The fast repriming kinetics and slow development of CSI of $Na_v1.3$ make it suitable for generating a large response to slowly developing depolarizing inputs (ramp stimuli)[40]. We first tested the effect of RTX-VII on the ramp current (I_{ramp}) of $Na_v1.3$ evoked by various ramp stimuli (Figure 3a p1). Consistent with previous studies[33], $Na_v1.3$ expressed in HEK293T cells produced a large inward Na^+ current in response to a linearly increasing voltage ramp from −100 mV to 20 mV at the ramp rate of 1.2 mV/ms; of the two I_{ramp} peaks shown, the first one (I_{ramp1}) but not the second one (I_{ramp2}) was ramp rate-dependent, with higher rate leading to larger I_{ramp1} (Figure 3b, *black trace*). The application of 0.5 μM RTX-VII increased the amplitude of both I_{ramp1} and I_{ramp2} generated by $Na_v1.3$ at all ramp rates tested along with a hyperpolarization shift of the initial activation voltage for I_{ramp1} (Figure 3b, *red trace*; the maximum tolerable voltage error was less than 5 mV, the mean maximum Rs-caused depolarizing voltage error was 3.45 ± 1.26 mV).The negative shift of I_{ramp1} of $Na_v1.3$ was consistent with the channels' negatively shifted activation. The enhanced activation of I_{ramp1} of $Na_v1.3$ may have been derived from the larger potential gradient (caused by the negative shift of activation voltage of I_{ramp1}) that drives Na^+ to cross the membrane as well as a slowed CSI which makes more channels available for activation.

$Na_v1.3$ intrinsically produces small I_{NaP}, and the relationship between I_{NaP} and I_{ramp2} was investigated in a previous study in which a close correlation between them was observed[33]. To clarify the relationship between the RTX-VII evoked I_{NaP} and I_{ramp2}, the protocol p2 described in Figure 3a was used to elicit two type currents of $Na_v1.3$ (Figure 3c). Note only I_{ramp2} could be evoked at the ramp rate of 0.2 mV/ms (Figure 3b and Figure 3c). RTX-VII dose-dependently enhanced I_{NaP} (I_{45ms}) and I_{ramp2} of $Na_v1.3$ (Figure 3c).The apparent EC_{50} for RTX-VII activating I_{ramp2} was 320 nM, as revealed by plotting I_{ramp2}/I_{NaT} ratios as a function of toxin concentrations (Figure 3d). This EC_{50} value did not differ much from that of RTX-VII activating the I_{NaP} of $Na_v1.3$ (120 nM). Furthermore, the correlation coefficient between I_{NaP} and I_{ramp2} was 0.9947 (Figure 3e), indicating a close correlation between them. Thus, data derived from the toxin study further confirmed the conclusion described above.

The effect of RTX-VII on the ramp current of Na_vs in neonatal hippocampal neurons was also examined. As shown in Figure 3f, both I_{ramp1} and I_{ramp2} of hippocampal Na_vs were evoked by a linearly increasing voltage ramp from −100 mV to 20 mV at the ramp rate of 1.2 mV/ms (Figure 3a, p3); both components of the I_{ramp} of hippocampal Na_vs were greatly enhanced by toxin (Figure 3f, *upper*). As shown in Figure 3f (*below*), both I_{ramp1} and I_{ramp2} of hippocampal Na_vs in control conditions displayed voltage-dependent inactivation by reverse ramp (R-ramp) stimulation following forward ramp (F-ramp) stimulation (Figure 3a, p4); as I_{ramp1} disappeared, the amplitude of I_{ramp2} decreased in the R-ramp compared with that in the F-ramp. On the contrary, 1 μM RTX-VII treatment removed the voltage-dependent inactivation of I_{ramp2} but not I_{ramp1}, as toxin induced a nearly unchanged I_{ramp2} in both the forward and reverse ramps, while I_{ramp1} was absent in the R-ramp. This finding indicates that the amplitude of I_{ramp2} in the presence of the toxin is only dependent on the transmembrane potential, and this population of Na_vs generating I_{ramp2} should maintain a continuous open state during the entire time course of AP. The toxin negatively shifted I_{ramp1} and the enhanced activation of I_{ramp2} might lower the threshold and increase the frequency of AP in hippocampal neurons, respectively, which possibly triggers the spontaneous AP firing in hippocampal neurons at a physiological resting potential. Current-clamp experiments showed that 2 μM RTX-VII triggered spontaneous high frequency AP firing in hippocampal neurons (Figure 3g, *upper*; Supplementary Fig. S3), a mechanism underlying toxin-induced seizure-like symptom in mice. By contrast, the spontaneous AP firing was rare in hippocampal neurons under control conditions (Figure 3g, *below*; Supplementary Fig. S3).

Domains II and IV of $Na_v1.3$ are critical for I_{NaP} generation by RTX-VII. Because $Na_v1.5$ is resistant to RTX-VII (Figure 4b), a chimera strategy was used to screen the critical modules [voltage sensor domains (VSD) or pore domains (PD)] responsible for the toxin-induced I_{NaP} of $Na_v1.3$. Each module from the four domains of $Na_v1.3$ was substituted with the corresponding $Na_v1.5$ module (Supplementary Fig. S4). The nomenclature of a specific chimeric channel was defined as follows: for example, $Na_v1.3/1.5$ DI-VSD chimera is a hybrid channel in which the DI-VSD of $Na_v1.3$ was replaced with that of $Na_v1.5$. Eight $Na_v1.3$ derived chimeric channels were constructed. All chimeric channels except the $Na_v1.3/1.5$ DII-VSD chimera were functionally expressed in HEK293T cells; therefore, the hybrid channel $Na_v1.3/1.5$ DII was generated instead of the $Na_v1.3/1.5$ DII-VSD chimera (Supplementary Fig. S4). To assess the potency and efficacy of RTX-VII for I_{NaP} generation in each wt- or chimeric channel, a 300-ms depolarization to 10 mV from a holding potential of −100 mV was applied to evoke the I_{NaT} and I_{NaP} of a specific channel in the absence and presence of various concentrations of

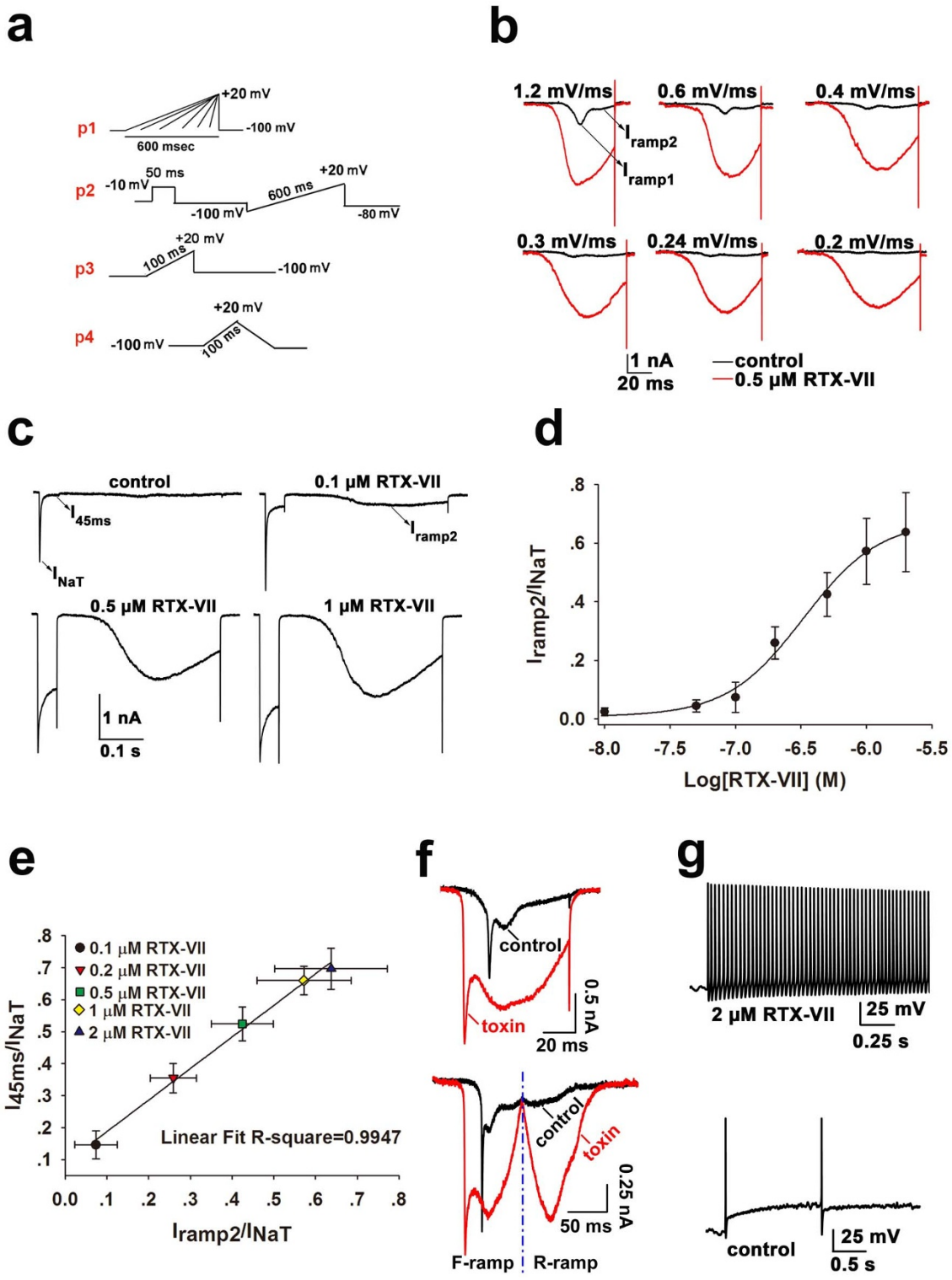

Figure 3 | The effects of RTX-VII on the ramp currents of $Na_v1.3$ and Na_vs of hippocampal neurons. (a) Protocols are used in the experiments described in this figure. (b) A series of inward $Na_v1.3$ currents are evoked by using linearly increasing ramp voltage from −100 mV to 20 mV with different ramp rate (Figure 3a, p1), the ramp time ranges from 100 ms to 600 ms, 100 ms/step. The $Na_v1.3$ ramp current (I_{ramp}) displays two peaks with the first one (I_{ramp1}) but not the second one (I_{ramp2}) being sensitive to ramp rate in control (*black traces*). 0.5 μM RTX-VII enhances the amplitudes of both peaks and causes a hyperpolarized shift of the initial activation voltage for I_{ramp1} (*red traces*); numbers labeled above the traces indicate the ramp rate (mV/ms) (n = 10). (c) Representative traces show that RTX-VII dose-dependently enhances the I_{NaP} (I_{45ms}) and I_{ramp2} of $Na_v1.3$ elicited by the protocol p2 shown in Figure 3a (n = 5). (d) Dose-response curve for RTX-VII activating the I_{ramp2} of $Na_v1.3$, the apparent EC_{50} is determined as approximate 0.3 μM; the maximum and the minimum response of $Na_v1.3$ to RTX-II is 63.03% and 2.15%, respectively (n = 5). (e) The I_{45ms}/I_{NaT} ratio was plotted as a function of the I_{ramp2}/I_{NaT} ratio at each toxin concentration (data from Figure 3c). A linear fit of the dots shows the close correlation between the I_{NaP} and I_{ramp2} of $Na_v1.3$ ($R^2 = 0.9947$) (n = 5). (f) Compared with control, 1 μM RTX-VII evidently enhances both peaks (I_{ramp1} and I_{ramp2}) of the ramp current of Na_vs in rat hippocampal neurons (*upper*). Protocol p3 shown in Figure 3a was used (n = 5); Representative traces (*below*) show that the I_{ramp} of Na_vs in hippocampal neurons is elicited by protocol p4 shown in Figure 3a (n = 5). (g) Spontaneous AP firing in a neonatal rat hippocampal neurons in the absence (*below*) and presence (*upper*) of 2 μM RTX-VII (n = 8).

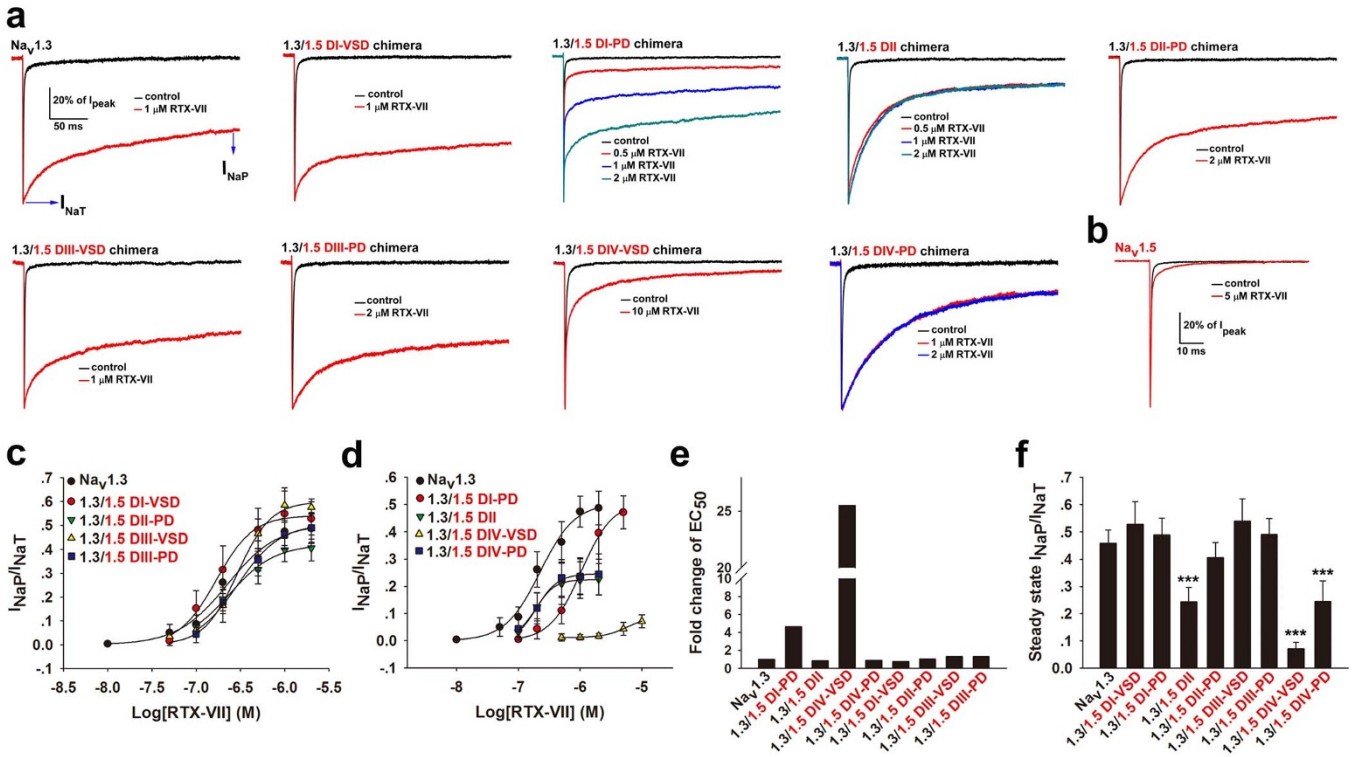

Figure 4 | Domain II and IV of Na$_v$1.3 are synergistically involved in I_{NaP} generation. (a) A 300-ms recording of currents of wt-Na$_v$1.3 and Na$_v$1.3 derived chimeric channels before and after the application of various concentration of RTX-VII. Chimeric channels were constructed as follows: the voltage-senor domain (VSD) or pore domain (PD) of DI, DII, DIII or DIV of Na$_v$1.3 was substituted with the corresponding domain of Na$_v$1.5 (see Supplementary Fig. S4). Here, I_{NaP} was measured at time point of 295 ms. Note DII, DIV-VSD, DIV-PD substitutions in Na$_v$1.3 results in the reduction of toxin induced I_{NaP} compared with wt- and other chimeric channels (n = 7–11). (b) Representative traces show that Na$_v$1.5 is resistant to RTX-VII (n = 4). (c) Dose-response curves for RTX-VII activating the I_{NaP} of wt-Na$_v$1.3 channel and Na$_v$1.3 derived chimeric channels that did not or slightly changed toxin potency (EC_{50}) or efficacy (steady-state I_{NaP}/I_{NaT} ratio at the saturated concentration of the toxin) (n = 7–11). (d) Dose-response curves for RTX-VII activating the I_{NaP} of wt-Na$_v$1.3 and chimeric channels that dramatically changed toxin potency and/or efficacy (n = 7–11). (e) Bars show the fold changes of the apparent EC_{50} of RTX-VII on each Na$_v$1.3 derived chimeric channel compared with that for wt-Na$_v$1.3 (n = 7–11). (f) Bars show ratios of the steady-state I_{NaP}/I_{NaT} of wt- and Na$_v$1.3 derived chimeric channels in the presence of the saturated concentration of toxin. These values are 45.88 ± 4.78%, 52.78 ± 8.32%, 48.87 ± 6.09%, 24.46 ± 5.27%, 40.64 ± 5.47%, 53.95 ± 8.13%, 49.00 ± 5.88%, 7.16 ± 2.33% and 24.48 ± 7.52% for the chimeric channels Na$_v$1.3, 1.3/1.5 DI-VSD, 1.3/1.5 DI-PD, 1.3/1.5 DII, 1.3/1.5 DII-PD, 1.3/1.5 DIII-VSD, 1.3/1.5 DIII-PD, 1.3/1.5 DIV-VSD and 1.3/1.5 DIV-PD, respectively (***$p < 0.001$, when compared with wt-1.3) (n = 7–11).

toxin, and the I_{NaP} was measured at the time point of 295 ms (Figure 4a) because the currents of chimeric channels reached a macroscopic steady state at the time point of 300 ms. To compare data derived from different channels, the relative values of I_{NaP}/I_{NaT} (both from the same current trace) after treatment with different concentrations of toxin were calculated, and the potency of RTX-VII on a specific channel was defined as the EC_{50} value, while the efficacy of RTX-VII was determined by steady-state I_{NaP}/I_{NaT} ratio at the saturated concentration of toxin.

The substitution of the VSD/PD of Na$_v$1.3 with that of Na$_v$1.5 had different effects on the potency and efficacy of RTX-VII. Compared with the wt-channel, five chimeric channels, namely Na$_v$1.3/1.5 DI-VSD, DI-PD, DII-PD, DIII-VSD and DIII-PD produced a large I_{NaP} in response to RTX-VII, whereas the other three chimeric channels, Na$_v$1.3/1.5 DII, DIV-VSD and DIV-PD displayed a smaller I_{NaP} (Figure 4a). The apparent EC_{50} values of RTX-VII on these channels were further determined from dose-response curves (Figure 4c and d). The bar diagrams shown in Figure 4e and f indicate the changes in the potency and efficacy of RTX-VII on Na$_v$1.3 derived chimeric channels, respectively, which could be described as follows: (1) in the chimeras Na$_v$1.3/1.5 DI-VSD, DII-PD, DIII-VSD and DIII-PD, no significant changes in the potency and efficacy of RTX-VII were observed, as indicated by the negligible reduction in the steady-state I_{NaP}/I_{NaT} ratios and the less than two-fold increments of EC_{50} values; (2) the chimera Na$_v$1.3/1.5 DI-PD generated a large steady-state I_{NaP}, similar to that of the wt-Na$_v$1.3; however, an approximate 4.8 fold increase of the EC_{50} value was observed, indicating that this chimeric channel reduced the binding affinity of RTX-VII but not the efficacy; (3) the chimeras Na$_v$1.3/1.5 DII and DIV-PD significantly decreased the efficacy of RTX-VII, as revealed by a significantly smaller steady-state I_{NaP}/I_{NaT} ratios (steady-state I_{NaP} only accounts for approximate 24% of I_{NaT} after 2 μM RTX-VII treatment, $P < 0.001$ when compared to wt-Na$_v$1.3); however, these substitution resulted in a < 2-fold increase of the EC_{50} values; (4) In the chimera Na$_v$1.3/1.5 DIV-VSD, both the potency and efficacy of RTX-VII was significantly attenuated, because the toxin, even at a concentration of 10 μM, induced a small fraction of steady state I_{NaP} (<10% of the I_{NaT}, $P < 0.001$, when compared to wt-Na$_v$1.3) in this chimeric channel and the apparent EC_{50} of toxin on this chimeric channel was increased by approximate 25 folds when compared to wt-Na$_v$1.3. Taken together, these findings suggest that DIV-VSD, DIV-PD, DII and DI-PD of Na$_v$1.3 play important roles in the RTX-VII-induced I_{NaP}. The different influence of these Na$_v$1.3 module substitutions on the potency and efficacy of RTX-VII suggest that they play different roles. DIV-VSD and DI-PD might jointly compose the binding receptor for RTX-VII, whereas the loss of efficacy of RTX-VII on the chimeric

channel $Na_v1.3/1.5$ DII was not caused by loss of toxin binding but was rather associated with an intrinsic limitation of this hybrid channel in generating a larger I_{NaP}.

Domain II of $Na_v1.3$ is not involved in interacting with RTX-VII. Further experiments were performed to clarify the roles of $Na_v1.3$ DII and DIV. First, we examined whether RTX-VII binds to $Na_v1.3$ DII. Neurotoxins acting on DII of Na_vs often cause a negative or positive shift of the activation kinetics of targeted channels[41]. The substitution of the DII of $Na_v1.3$ with that of $Na_v1.5$ should affect the RTX-VII-induced negative shift of activation kinetics of $Na_v1.3$ if the toxin binds to $Na_v1.3$ DII, as RTX-VII did not affect the I–V curve of $Na_v1.5$ (Supplementary Fig. S5a). Therefore, the activation kinetics of the chimeric channel $Na_v1.3/1.5$ DII was investigated before and after the application of 2 μM RTX-VII. RTX-VII negatively shifted the voltage-dependent activation of the $Na_v1.3/1.5$ DII chimera and increased the I_{NaT} at voltages ranging from −50 mV to 5 mV (Figure 5a). In addition, 2 μM RTX-VIII caused an approximate 14 mV negative shift of the G–V curve of the $Na_v1.3/1.5$ DII chimera without changing the slope factor ($V_a = -18.00 \pm 1.71$ mV for control and $V_a = -32.09 \pm 1.99$ mV for the toxin treatment; $K_a = 7.23 \pm 1.22$ mV for control and $K_a = 6.82 \pm 1.30$ mV for the toxin treatment; the maximum tolerable voltage error was less than 5 mV, the mean maximum Rs-caused depolarizing voltage error was 2.92 ± 2.10 mV, $p < 0.001$ when compared to the *Va* shifted amplitude) (Figure 5b).This raises the possibility that the toxin might not interact with $Na_v1.3$ DII, which was further confirmed by using a competitive assay. HNTX-III is a tarantula toxin that inhibits the I_{NaT} of $Na_v1.3$ and $Na_v1.7$. It was found that this toxin targeted DII S3–S4 linker of Nav1.7[42]. The wt-Nav1.5 channel and the $Na_v1.3/1.5$ DII chimera were resistant to 1 μM HNTX-III treatment, whereas the $Na_v1.3/1.5$ DII-PD chimera was inhibited by 1 μM HNTX-III (Supplementary Fig. S5 b–d). Reconstruction of the DII of Nav1.3 to Nav1.5 (Na_v 1.5/1.3 DII chimera) conferred the inhibitory activity of HNTX-III to this channel (Supplementary Fig. S5 e).These evidences indicate HNTX-III inhibit Nav1.3 by binding to its DII-VSD. If RTX-VII also targeted DII-VSD of $Na_v1.3$, its binding should prevent the interaction of HNTX-III with $Na_v1.3$ because of steric hindrance, which would result in an attenuation of the inhibitory potency of HNTX-III on $Na_v1.3$. As shown in Figure 5c, the inhibitory effects of HNTX-III on $Na_v1.3$ I_{NaT} did not differ between 0.5 μM RTX-VIII-pretreated and -untreated channels. The dose-response curves were also superimposed well (Figure 5d), providing evidence to rule out the binding of RTX-VII to $Na_v1.3$ DII. Next, we determined the molecular determinant in DIV of $Na_v1.3$ for RTX-VII binding. Since $Na_v1.5$ is resistant to RTX-VII, the residues in S1–S2 and S3–S4 extracellular loops of $Na_v1.3$ were mutated to the corresponding residues of $Na_v1.5$, respectively (Figure 5e). A total of seven residues were mutated and six of them were functionally expressed except V1566F. The kinetics for the activation and SSI of all mutants were listed in supplementary Table S1. Compared with wt-$Na_v1.3$, Four mutant channels (K1503P, M1505K, T1506I, L1507N) carrying mutations in the S1–S2 linker led to a 4–12 folds increase of apparent EC_{50} values, whereas the E1562Q and E1562R mutation in the S3–S4 linker resulted in an approximate 5 folds and 20 folds increase of the apparent EC_{50} values (Figure 5f and 5g). These data indicate that multiple residues located in $Na_v1.3$ DIV were involved in interacting with RTX-VII, and that E1562 was the most important residue for the interaction.

Reverse reconstruction of $Na_v1.3$ DII and DIV into $Na_v1.5$ fully restores toxin efficacy. Considering the critical role of the DII and DIV of $Na_v1.3$ in the RTX-VII-induced I_{NaP}, we assumed that reverse reconstruction of $Na_v1.3$ DII and DIV into $Na_v1.5$ might restore the efficacy of the toxin. A reversal chimeric strategy was used as follows: four domains of $Na_v1.3$ were stepwise reconstructed into the scaffold of $Na_v1.5$ (Supplementary Fig. S6). The nomenclature of a chimeric channel was defined as follows: for example, $Na_v1.5/1.3$ DI was a chimeric channel in which the DI of $Na_v1.5$ was substituted with that of Nav1.3. A total of 11 chimeric channels were constructed and their I_{NaP} generation by the toxin was compared. Again, I_{NaP} was measured at the time point of 295 ms (Figure 6a). The substitution of all four domains of $Na_v1.5$ with those of $Na_v1.3$ (Nav1.5/1.3 DI-II-III-IV) almost fully restored the efficacy of RTX-VII, thus eliminating the involvements of the intracellular loops of $Na_v1.3$ in the toxin-induced I_{NaP}. Of the four single domain replaced chimeric channels, $Na_v1.5/1.3$ DI, $Na_v1.5/1.3$ DII and $Na_v1.5/1.3$ DIII chimeras were resistant to RTX-VII, similar to wt-$Na_v1.5$, whereas $Na_v1.5/1.3$ DIV chimera was sensitive to RTX-VII. Furthermore, the toxin slowed the inactivation and induced a small steady- state I_{NaP} in this chimeric channel, indicating that $Na_v1.3$ DIV is important but not sufficient for RTX-VII inducing large I_{NaP}. Of the two triple domain replaced chimeric channels, $Na_v1.5/1.3$ DI-III-IV chimera did not fully restore toxin efficacy but $Na_v1.5/1.3$ DI-II-IV chimera did, which indicates that the DII but not the DI and DIII of $Na_v1.3$ is required for toxin inducing large I_{NaP}. Of the three double domain replaced chimeric channels, the reconstruction of the DI or DIII of $Na_v1.3$ into the scaffold of $Na_v1.5/1.3$ DIV chimera ($Na_v1.5/1.3$ DIII-IV chimera or $Na_v1.5/1.3$ DI-IV chimera) had a limited effect on restoring toxin efficacy, whereas the reconstruction of the DII of $Na_v1.3$ into $Na_v1.5/1.3$ DIV chimera (Nav1.5/1.3 DII-IV chimera) almost fully rescued toxin efficacy, suggesting the assembly of the DII and DIV of $Na_v1.3$ should be sufficient for RTX-VII inducing large I_{NaP}. Additionally, the chimeric channel $Na_v1.5/1.3$ DI-III-IV&DII PD, where only the DII-PD but not the whole DII of $Na_v1.3$ was present, also attenuated the efficacy of RTX-VII compared with that of $Na_v1.5/1.3$ DI-II-III-IV chimera, which strongly supports that the DII-VSD of $Na_v1.3$ plays a vital role in toxin-induced I_{NaP} generation.

The apparent EC_{50} values of RTX-VII on the $Na_v1.5$ derived chimeric channels containing $Na_v1.3$ DIV were estimated from the dose-response curves (Figures 6b and c), and the changes in the potency and efficacy of RTX-VII on these chimeric channels were showed in Figures 6d and e, respectively. Of the $Na_v1.3$ DIV-containing chimeric channels, the $Na_v1.3$ DII-containing ones ($Na_v1.5/1.3$ DI-II-III-IV, DI-II-IV and DII-IV chimeras), but not those without reconstruction of $Na_v1.3$ DII or DII-VSD ($Na_v1.5/1.3$ DIV, DI-III-IV, DI-IV and DI-III-IV&II-PD chimeras), produced a large steady-state I_{NaP} comparable to that of wt-$Na_v1.3$ in the presence of saturated concentration toxin (Figure 6e). On the other hand, the toxin potency on these $Na_v1.3$ DIV-containing chimeric channels were only slightly weaker than that of wt-$Na_v1.3$, although the greatest fold change of EC_{50} was observed in $Na_v1.5/1.3$ DII-DIV chimera (8 folds) (Figure 6d). Moreover, the incorporation of $Na_v1.3$ DI into $Na_v1.5/1.3$ DII-DIV chimera ($Na_v1.5/1.3$ DI-DII-DIV chimera) led to an evident enhancement of toxin potency, which is comparable to that of wt-$Na_v1.3$ channel. The results are consistent with the interpretation that the DIV of $Na_v1.3$ was the main toxin binding site, while the DI-PD of $Na_v1.3$ might construct the low affinity binding site for RTX-VII. Overall, combining data in Figures 4 and 6 confirmed the cooperative involvement of DII and DIV in the toxin-induced I_{NaP} of $Na_v1.3$.

Discussion

Neurotoxins produced by venomous animals, plants, and microorganisms are a valuable pool of molecular probes to investigate the structure-function relationship of Na_vs[43]. RTX-VII robustly enhances the I_{NaP} of $Na_v1.3$ and discriminates Na_v subtypes $Na_v1.4$, $Na_v1.5$, and $Na_v1.7$–1.9 from $Na_v1.3$. The toxin-induced and the intrinsic I_{NaP} share some common features, such as sub-threshold activation, a close correlation with I_{ramp2}, and triggering spontaneous high frequency AP firing. Furthermore, the brief late

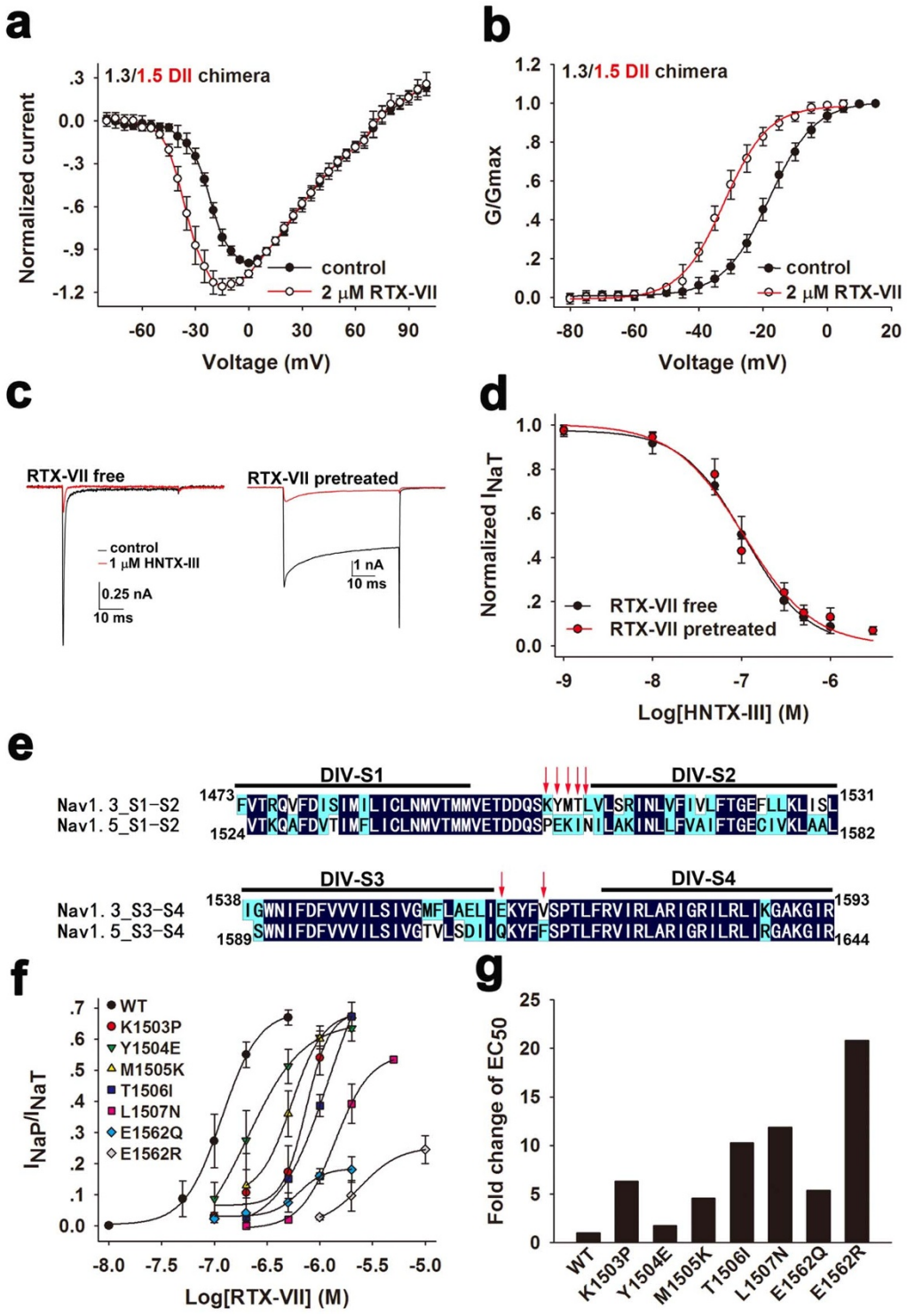

Figure 5 | Domain IV but not domain II of $Na_v1.3$ is involved in interacting with RTX-VII. (a) The I–V curves of $Na_v1.3/1.5$ DII chimera before and after 2 μM RTX-VII treatment (n = 6). (b) 2 μM RTX-VII negatively shifts the G–V curve of $Na_v1.3/1.5$ DII chimera without changing the slope factor ($V_a = -18.00 \pm 1.71$ mV for control and $V_a = -32.09 \pm 1.99$ mV for the toxin treatment; $K_a = 7.23 \pm 1.22$ mV for control and $K_a = 6.82 \pm 1.30$ mV for the toxin treatment) (n = 6). (c) Representative traces show 1 μM HNTX-III indiscriminately inhibits the I_{NaT} of 0.5 μM RTX-VII-untreated- (*RTX-VII free*) and -treated- (*RTX-VII pretreated*) $Na_v1.3$ channel (n = 5). HNTX-III was dissolved in bath solution containing 0.5 μM RTX-VII. (d) The dose-response curve for HNTX-III inhibiting the I_{NaT} of 0.5 μM RTX-VII-treated or -untreated $Na_v1.3$ channel shows that the potency of HNTX-III on both types of channel are the same (n = 5). The fractions which are resistant to the high dose of HNTX-III treatment account for 5.12% and 6.77% of the maximum I_{NaT}, respectively. (e) Sequence alignment of the DIV-VSD of $Na_v1.3$ and $Na_v1.5$, red arrows indicate amino acid residues in $Na_v1.3$ which were mutated to their counterpart in Nav1.5. (f) Dose-response curves for RTX-VII enhancing the I_{NaP} of $Na_v1.3$ mutants shown in Figure 5e demonstrate molecular determinants in $Na_v1.3$ for interacting with RTX-VII (n = 5–8); the apparent EC_{50} values are 117.73 nM, 741.48 nM, 208.83 nM, 541.00 nM, 1209.76 nM, 1399.27 nM, 635.04 nM, 2451, 32 nM for wt-$Na_v1.3$, K1503P, Y1504E, M1505K, T1506I, L1507N, E1562Q and E1562R, respectively. (g) Bars show the fold changes of apparent EC_{50} values of RTX-VII for mutants compared with that for wt-$Na_v1.3$ channel (n = 5–8).

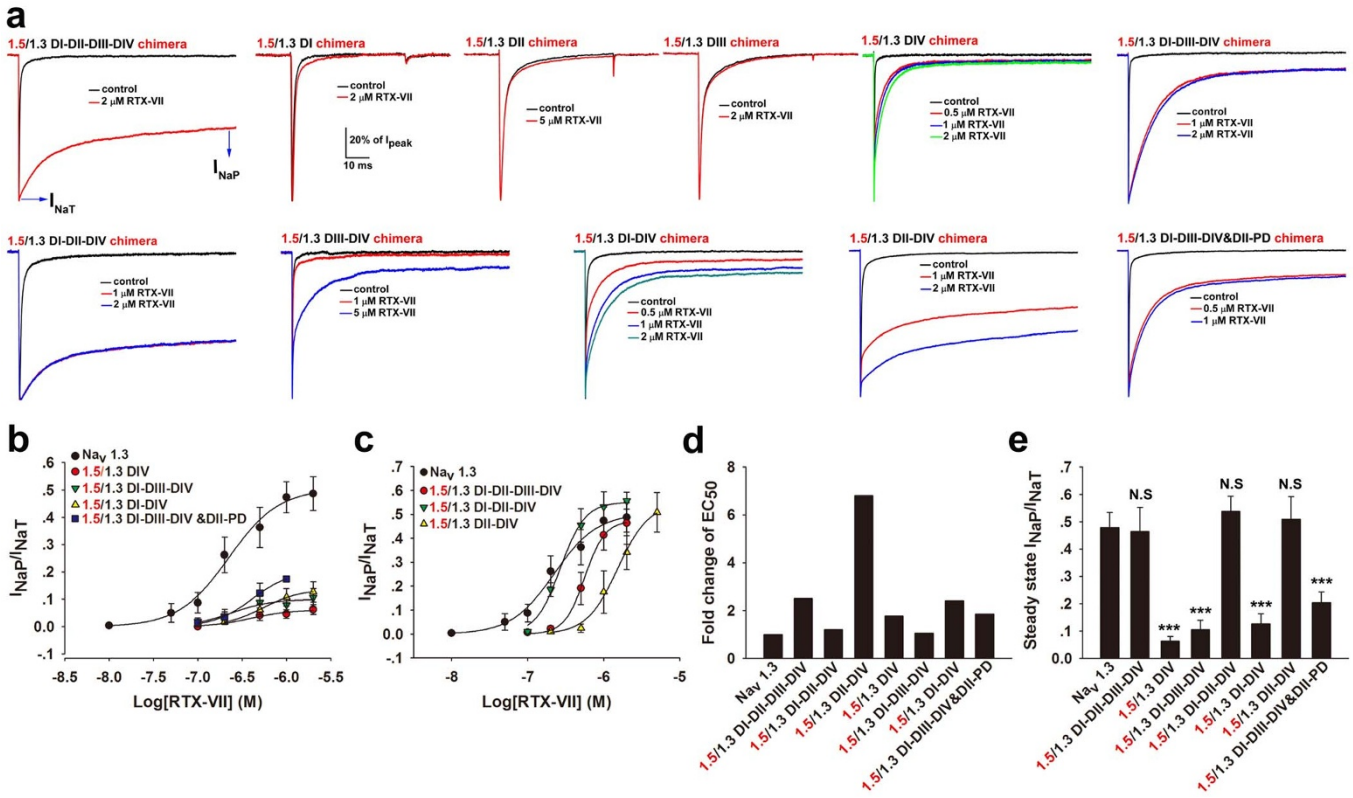

Figure 6 | The substitution of the domain II and IV of $Na_v1.5$ with those of $Na_v1.3$ restores RTX-VII efficacy. (a) A 300-ms recording of the currents of $Na_v1.5$ derived chimeric channels in the absence and presence of various concentration of RTX-VII (n = 6–9). The chimeric channels were constructed as follows: one or several domains (DI, DII, DIII or DIV) of $Na_v1.5$ were substituted with the corresponding domain/s of $Na_v1.3$ (see Supplementary Fig. S6). (b) Dose-response curves for RTX-VII enhancing the I_{NaP} of wt-$Na_v1.3$ and $Na_v1.5$ derived chimeric channels that did not or slightly restored toxin efficacy (steady-state I_{NaP}/I_{NaT} ratio at the saturated concentration of toxin) (n = 6–9). (c) Dose-response curves for RTX-VII enhancing I_{NaP} of wt-$Na_v1.3$ and $Na_v1.5$ derived chimeric channels that almost completely restored toxin potency and/or efficacy (n = 6–9). (d) Bars show the fold changes of the apparent EC_{50} of RTX-VII for each $Na_v1.5$ derived chimeric channels compared with that for wt-$Na_v1.3$ (n = 6–9). (e) Bars show the steady- state I_{NaP}/I_{NaT} ratio of wt-$Na_v1.3$ and $Na_v1.5$ derived chimeric channels in the presence of saturated concentrations of toxin. This values are 47.92 ± 5.43%, 46.37 ± 8.87%, 6.3 ± 1.82%, 10.60 ± 3.32%, 53.81 ± 5.56%, 12.68 ± 3.67%, 50.88 ± 8.33 and 20.41 ± 3.90% for $Na_v1.3$, 1.5/1.3 DI-DII-DIII-DIV, 1.5/1.3 DIV, 1.5/1.3 DI-DIII-DIV, 1.5/1.3 DI-DII-DIV, 1.5/1.3 DI-DIV, 1.5/1.3 DII-DIV and 1.5/1.3 DI-DIII-DIV&DII-PD, respectively (***$p < 0.001$, N.S = not significant, when compared with wt-$Na_v1.3$) (n = 6–9).

opening and burst of openings of Na_vs may be the common mechanism underlying the origin of both types of I_{NaP}. However, the intrinsic I_{NaP} of Na_vs is small, which hampered the investigation of the mechanism underlying I_{NaP} generation. RTX-VII dramatically enhancing the I_{NaP} of $Na_v1.3$ enabled detailed investigations of $Na_v1.3I_{NaP}$ generation. In the present study, we clarified the roles of the four domains of $Na_v1.3$ in I_{NaP} generation by using RTX-VII as a molecular probe.

Along with the enhancement of I_{NaP}, RTX-VII also facilitates $Na_v1.3$ channel opening at weak depolarizations as revealed by the toxin potentiating I_{NaT} of $Na_v1.3$ when depolarizing voltages are below 10 mV as well as the toxin negatively shifting channel's steady-state activation. This observation is not without precedent, as some α-scorpion toxins modulate Na_vs in a similar way[37]. This phenomenon could be reasonably interpreted as an increase of the maximum opening probability of the toxin-treated channels. However, how the toxin-bound channels open with a greater probability at weak depolarizations remains unclear. Our data indicate that RTX-VII binds to the DIV-VSD instead of the DII-VSD of $Na_v1.3$, which suggests that the potentiation of $Na_v1.3$ activation by the toxin might not derive from the toxin facilitating DII activation. Two possible explanations for RTX-VII enhancing the I_{NaT} of $Na_v1.3$ are proposed: (1) toxin treatment altered single channel conductance[44] of $Na_v1.3$. This interpretation seems unreasonable because the toxin does not alter the inward and outward Na^+ current of $Na_v1.3$ evoked by strong depolarizing voltages above 10 mV; (2) RTX-VII tends to stabilize the DIV-VSD of $Na_v1.3$ in a partially activated state (pre-activated state), which is required for channel activation but not sufficient to trigger channel inactivation (the fully activated DIV-VSD is required for the fast inactivation of Na_vs)[45], thus promoting channel activation in a similar but not identical way with that of β-scorpion toxins[46,47]. The vital difference is that β-scorpion toxins trap the DII-VSD but not DIV-VSD of Na_vs in the activated state. The latter interpretation seems plausible as emerging evidences support DIV is involved in Na_v activation[45,48]. Furthermore, the voltage driving the outward movement of DIV-VSD is the later step in the activation sequence of Na_vs[49]. RTX-VII did not alter the I_{NaT} of $Na_v1.3$ at strong depolarizing voltages (>10 mV), and this phenomenon could be interpreted by the fact that both toxin-free and toxin-bound channels in cell membrane are almost fully activated at 10 mV, which is in consistent with the G-V relationship observed in figure 2d. Taken in all, considering RTX-VII promoting activation and inhibiting inactivation of $Na_v1.3$ as well as the unique role of DIV-VSD in channel gating, we would like to suggest that RTX-VII might tend to trap and stabilize the DIV-VSD of $Na_v1.3$ in the pre-activated state during channel activation.

The reconstruction of $Na_v1.3$ DII but not DI or DIII to $Na_v1.5/1.3$ DIV chimera fully restored toxin efficacy, but it is interesting that RTX-VII did not bind to $Na_v1.3$ DII. Therefore, the role of this domain in the toxin-induced I_{NaP} remains unclear. Previous studies

showed that the inter-domain interactions of Na_vs is necessary for channel gating[50,51]. We proposed in this study that the DII and DIV of $Na_v1.3$ might cooperate to trigger late brief opening and burst of opening to generate I_{NaP}, and RTX-VII should facilitate/amplify this cooperation to induce large I_{NaP} in $Na_v1.3$. The subtle amino acid sequence differences of the domain II between $Na_v1.3$ and $Na_v1.5$ greatly affect this cooperation, namely the DII of $Na_v1.3$ can cooperate well with its own DIV, which is not the case for the DII of $Na_v1.5$ with DIV of $Na_v1.3$. The roles of $Na_v1.3$ DI and DIII of in the toxin-induced I_{NaP} generation were unclear. The fact that the replacement of the DI or DIII of $Na_v1.3$ with that of $Na_v1.5$ did not affect toxin efficacy could not exclude the possibility that both domains might involve in the I_{NaP} generation, because high sequence similarity of DI and DIII between $Na_v1.3$ and $Na_v1.5$ is observed and probably the inter-domain interactions might not be interfered although these two domains were replaced.

RTX-VII induced large I_{NaP} in $Na_v1.3$ at the end of a 50-ms or a 300-ms depolarization, which differs from some scorpion toxins and sea anemone toxins that slow the inactivation of Na_vs but the resultant current decay rapidly in 50 ms (Lqh2 as a representative[52]). What is the difference derived from? Theoretically, Lqh2 trapping the DIV-VSD of Na_vs in the closed state should have induced large I_{NaP}, but the fact is not. How are the toxin-bound channels inactivated? Slow inactivation may not be the underling mechanism. This is because that slow inactivation is rarely observed in a 50 ms depolarization (such a short depolarization is not sufficient to trigger this gating process). The repriming kinetics of the toxin-bound channels is the same as or even faster than that of the toxin-free channels[37], which is also inconsistent with the fact that the recovery of Na_vs from slow inactivation is slow[53]. Based on the unique role of DIV in fast inactivation, a model was proposed to clarify these two problems. Macroscopically, in this model, a depolarization would drive and maintain the first three domains of Na_vs in an activated state; Lqh2 and RTX-VII could trap the DIV-VSD of Na_vs in the closed[52] and partially activated state, respectively. For Lqh2, such trapping is not very stable, as the depolarization prolongs, the toxin-bound DIV-VSD would be gradually activated, triggering channel inactivation. However, for RTX-VII, the DII of $Na_v1.3$ might allosterically slow/inhibit this process, which therefore makes RTX-VII stably trap the DIV-VSD of $Na_v1.3$ in the partially activated state and then the channels would maintain a persistent opening state. The understanding of this process in the single channel level could be as follows: the inactivation ball of a Na_v has a "on state" (blocking the pore) and an "off state" (free in cytosol) which are tightly coupled to the activated and resting state of DIV-VSD, respectively[8]. Normally, DIV-VSD is immobilized in an outward conformation by activation[54,55]. The toxin-bound DIV-VSD could be activated by strong depolarization but not be stably immobilized as toxins tend to "drag" the DIV-VSD to its resting state (partially activated state for RTX-VII). Thus, when the toxin-bound DIV-VSD is activated, the inactivation ball is in the "on state" and the pore is occluded; when the toxin-bound DIV-VSD is in the resting state (partially activated state for RTX-VII), the channel just opens. The inactivation ball switches between the "on state" and the "off state" quickly and such inactivation ball movement should trigger the burst opening of the channel in single channel recording. For Lqh2, as the depolarization prolonged, the DIV-VSD of most channels would be stably immobilized and these channels were consequently trapped stably in the inactivated state. On the other hand, for RTX-VII, toxin binding to the DIV-VSD of $Na_v1.3$ should allosterically affect the conformation of DII-VSD, which would in turn interfere with the time-dependent immobilization of DIV-VSD. We proposed that such gating model underlies the generation of large I_{NaP} in $Na_v1.3$ by RTX-VII.

Methods

Venom and toxin purification. Spider *Macrothele raveni* were collected in GuangXi province, China. The spider has a body length of 3–5 cm and the venom was collected by an electric stimulation method as described in another work of our laboratory[34]. The collected crude venom was lyophilized and preserved at −80°C before use. The crude venom was dissolved in ddH_2O to a final concentration of 5 mg/ml and subjected to the first round of RP-HPLC purification (acetonitrile gradient: 1%–60%, at an increasing rate of 1% per minute). The fraction containing RTX-VII was then collected, lyophilized and subjected to the second round of RP-HPLC with a slower increasing acetonitrile gradient (acetonitrile at an increasing rate of 0.5% per minute) to obtain the purified toxin.

Toxin sequencing and cDNA of RTX-VII. Partial amino acid sequence of RTX-VII was determined by Edman degradation on an Applied Biosystems/PerkinElmer Life Science Procise 491-A protein sequencer. The cDNA of this toxin was obtained by blasting Edman degradation determined amino acid sequence of RTX-VII against the local cDNA library database of the spider *Macrothele raveni* (unpublished data).

Constructs and transfection. All Na_v clones and beta subunit clones were kindly gift from Dr Theodore R.Cummins (Department of pharmacology and Toxicology, Stark Neurosciences Research Institute, Indiana University School of Medicine, USA). cDNA genes encoding rat $Na_v1.3$ and rat $Na_v1.4$ were subcloned into the vectors pcDNA3.1 and pRGB4[40,56], respectively; the cDNA genes encoding human $Na_v1.5$ and human $Na_v1.7$ were subcloned into the vectors pcDNA3.1 and pcDNA3.1-mod[57], respectively. Auxiliary β1 and β2 subunits both were cloned from human and inserted into an internal ribosome entry site vector[58]. All site mutations of $Na_v1.3$ were constructed by using the QuikChange II XL Site-directed Mutagenesis kit (Agilent Technologies) according to the manufacture's instruction. The cytosolic boundaries of two adjacent transmembrane segments and two adjacent domains of $Na_v1.3$ or $Na_v1.5$ were determined by proteins' topological information deposited in NCBI protein database (for $Na_v1.3$, the website is http://www.ncbi.nlm.nih.gov/protein/NP_037251.1, and for $Na_v1.5$,the website link is http://www.ncbi.nlm.nih.gov/protein/NP_932173.1). The protein sequence location of each voltage sensor (VSD)/pore domain (PD) of all four domains of $Na_v1.3$ and $Na_v1.5$ are as listed in Supplementary Table S4. A homologous recombination strategy was employed to generate the chimeric channels using the In-Fusion®HD Cloning kit (Clontech Laboratories) or CloneEZ® PCR Cloning kit (Genscript). For example, for the construction of $Na_v1.3/1.5$ DI-VSD chimera, the DI-VSD (voltage sensor of domain I) of $Na_v1.5$ was amplified by PCR using a pair of primers with their 5′ end extended by a 15 bp long joint which is homologous or reverse compliment to the upstream or downstream flanking sequence of DI-VSD of $Na_v1.3$. A pair of oppositely directed primers was used to linearize the whole $Na_v1.3$ cloned plasmid with the DI-VSD of $Na_v1.3$ deleted. The PCR amplified segment and the linearized plasmid were subjected to 1% agarose gel electrophoresis, respectively. The corresponding bands were recycled using a DNA gel extraction kit (Sangon biotech) and ligated using the In-Fusion®HD Cloning kit (Clontech Laboratories) or CloneEZ® PCR Cloning kit (Genscript). Before being transformed to E.coli Top10 competent cell, the ligated product was subjected to FastDigest DpnI (Thermo Scientific) treatment at 37°C for 1 hour to remove the template plasmid. The transformants were verified by colony-PCR using a pair of gene specific primer for each inserted segment and then sequencing (Genscript). The primers used for vector linearization and amplification of Na_v domains were listed in Supplementary Table S2 and Table S3. HEK293T cells (ATCC) were grown under the standard cell culture conditions (5% CO_2 and 37°C) in Dulbecco's Modified Eagle Medium (DMEM, Life technologies) supplemented with 10% fetal bovine serum. These Na_v constructs were co-transfected with plasmid containing β1 subunit and PEGFP-N1 to HEK293T cells using Lipofectamine 2000 (Life Technology) according to the manufacture's instruction. For wt-$Na_v1.3$, $Na_v1.3$ mutants and $Na_v1.3$ derived chimeric channels, 3 μg Na_v plasmid, 1 μg plasmid containing β1 subunit and 0.5 μg PEGFP-N1 plasmid were co-transfected. For wt-$Na_v1.5$ and $Na_v1.5$ derived chimeric channels, 1 μg Na_v plasmid, 0.3 μg plasmid containing β1 subunit and 0.5 μg PEGFP-N1 plasmid were co-transfected. For ramp test, $Na_v1.3$ was co-transfected with plasmid containing β1 subunit and plasmid containing β2 subunit[33]. Cells were 80%–90% confluent before transfection, and cells were seeded on a poly-lysine coated Microscope Cover Glass (Fisher scientific) 4–6 hours after transfection. 24 hours after seeding, cells were ready for patch-clamp analysis.

Primary culture of DRG and hippocampal neurons and toxicity test of animals. Animals (Sprague-Dawley rats and Kunming mice) were used according to the guidelines of the National Institutes of Health for care and use of laboratory Animals. The experiments were approved by the Animal Care and Use Committee of the College of Medicine, Hunan Normal University. Acutely dissociated dorsal root ganglion (DRG) cells were prepared from 4 weeks old Sprague-Dawley rats and maintained in short-term primary culture using the method described by Hu, H.Z and Li, Z.W[59]. The dissociated cells were suspended in DMEM supplemented with 10% fetal bovine serum, 50 IU/ml penicillin, and 50 μg/ml streptomycin. Cells were seeded on poly-L-lysine-coated Microscope Cover Glass placed in a cell culture dish (35 × 10 mm, corning) and incubated at 37°C in an atmosphere of 5% CO_2. Cells cultured for 3–24 h were used in the patch experiments. Experiments were conducted at room temperature (20–25°C). For primary culture of hippocampal neurons, hippocampal tissues of neonatal rats were dissected and treated with 0.25% trypsin in Ca^{2+}-Mg^{2+}-free Hank's Buffered Salt solution at 37°C for 15 min, and then were dissociated by trituration with glass Pasteur pipette and seeded on poly-L-lysine-coated Microscope Cover Glass placed in a cell culture dish (35 × 10 mm, corning). Approximate 3.5*10^4 cells in DMEM containing 10% fetal bovine serum were plated in each dish. The culture medium were replaced with serum-free Neurobasal®

medium (Life technologies) supplemented by 2% B27 (Life technologies) on the second day after plating, 500 μM glutamine was added to reduce the growth of glial cells. The hippocampal neurons were maintained in a CO_2 incubator at 37°C, one-half volume of the culture medium was replaced with fresh medium every other day. The neurons were used for patch-clamp analysis after they were maintained in culture for 14–17 days. In order to test the neurotoxicity of RTX-VII, ten mice of either sex with an average weight of 20 g were randomly divided to two groups, animals in the control group were intracerebroventricularlly injected with 20 μL saline, and animals in the experimental group were injected with 20 μL saline containing 20 ng toxin.

Electrophysiology. Cell current recording was made with the whole-cell patch-clamp technique using an EPC 10 USB Patch Clamp Amplifier (HEKA Elektronik). Cells transfected with wt/mutant/chimeric Na_v channels and DRG/hippocampal neurons seeding in a glass coverslip were placed in a perfusion chamber in which rapid exchange of solutions around cells could be performed. The recording pipettes were made from glass capillary (thickness = 0.225 mm) using a PC-10 puller (NARISHIGE).The pipet resistance was controlled at 1.5–2.0 MΩ by adjusting the pulling temperature. The standard pipet solution contained (in mM): 140 CsCl, 10 NaCl, 1 EGTA, 2 Mg-ATP, and 20 HEPES (pH 7.4). Bath solution contained (in mM): 140 NaCl, 2 $CaCl_2$, 1 $MgCl_2$, 5 KCl, 20 HEPES (pH 7.4), and 10 glucose. All experiments were conducted at the room temperature (20–25°C). All chemicals were the products of SigmaAldrich and dissolved in water. Data were acquired by PatchMaster software (HEKA Elektronik). Data were analyzed by softwares Igo Pro 6.10A, Excel 2010, Sigmaplot 10.0 and OriginPro 8. Voltage errors were minimized by using 80% series resistance compensation, the speed value of Rs compensation was set to be 10 μs(fast compensation).The capacitance artifact were canceled using the computer-controlled circuitry of the patch clamp amplifier. The pipet capacitance was minimized by filling the pipet with small volume of pipet solution, and the pipet capacitance was controlled to be <10 pF for effective automatic compensation by EPC-10 amplifier. The pipet capacitance and the cell capacitance was sequentially compensated after the seal and the whole-cell configuration was established, respectively(pipet capacitance and cell capacitance was compensated by automatic fast and slow capacitance compensation, respectively).Stock solution of RTX-VII (1 mM in sterile ddH_2O) was diluted with fresh bath solution to a concentration of 10 folds of the interested concentration, 30 μL of the concentrated toxin was diluted into the recording chamber (containing 270 μL bath solution) far from the recording pipet (the recording cell) and was mixed by repeatedly pipetting to achieve the specified final concentration[60]. The dose-response curves of toxin on wt/mutant/chimeric channel were fitted to a Hill equation to estimate the potency of toxin (EC_{50}). The G-V curve before and after toxin treatment and the steady state inactivation (SSI) curve before toxin treatment were fitted using a boltzmann equation: $y = 1/(1 + \exp[(V_{1/2} - V)/K])$ in which $V_{1/2}$, V, and K represented midpoint voltage of kinetics, test potential and slope factor, respectively. The SSI curve after toxin treatment was fitted with a modified Boltzmann equation: $(Y - Y_{min})/(Y_{max} - Y_{min}) = 1/(1 + \exp[(V_{1/2} - V)/K])$, Y_{max} and Y_{min} represent the maximum and minimum responses. The time course curve for the I_{NaP} enhancement in response to the toxin application was best fitted by a single exponential rising equation ($y = y_0 + a(1 - e^{-x/\tau})$) and the time course for recovery of I_{NaP} upon bath solution washing was best fitted by a single exponential decay equation($y = y_0 + ae^{-x/\tau}$), here τ represent the time constant for toxin binding to and washing off from channels respectively. In measuring the spontaneous AP firing of neonatal rat hippocampal neuron using current-clamp, the pipette solution contains (in mM): 140 KCl, 5 $MgCl_2$, 5 EGTA, 2.5 $CaCl_2$, 4 ATP, 0.3 GTP, and 10 Hepes, pH 7.3 (adjusted with KOH). The bath solution contains (in mM): 140 NaCl, 1 $MgCl_2$, 5 KCl, 2 $CaCl_2$, 10 HEPES, and 10 glucose, pH 7.3 (adjusted with NaOH). During the recording, no current was injected to neurons.

Data analysis. Data were presented as Mean ± SD. n is presented as the number of the separate experimental cells. Dose response curves were fitted using the following Hill logistic equation: $y = f_{max} - (f_{max} - f_{min})/(1+([Tx]/EC_{50})^n)$, where f_{max} and f_{min} represent the maximum and minimum response of channel to toxin, [Tx] represent the toxin concentration, n is an empirical Hill coefficient. The Hill coefficient was set to 1 except where indicated otherwise. This is reasonable based on our mutagenesis analysis, which indicated a single high affinity binding site in $Na_v1.3$ for RTX-VII. Statistical significance was assessed with Microsoft excel 2010 using One-Way ANOVA. Statistical significance was accepted at *P* values less than 0.05.

1. Catterall, W. A. Voltage-gated sodium channels at 60: structure, function and pathophysiology. *J Physiol* **590**, 2577–89 (2012).
2. Catterall, W. A. From ionic currents to molecular mechanisms: the structure and function of voltage-gated sodium channels. *Neuron* **26**, 13–25 (2000).
3. Bosmans, F., Martin-Eauclaire, M. F. & Swartz, K. J. Deconstructing voltage sensor function and pharmacology in sodium channels. *Nature* **456**, 202–8 (2008).
4. Catterall, W. A. Structure and function of voltage-gated sodium channels at atomic resolution. *Exp Physiol* **99**, 35–51 (2014).
5. Yu, F. H. & Catterall, W. A. Overview of the voltage-gated sodium channel family. *Genome Biol* **4**, 207 (2003).
6. Catterall, W. A., Goldin, A. L. & Waxman, S. G. International Union of Pharmacology. XLVII. Nomenclature and structure-function relationships of voltage-gated sodium channels. *Pharmacol Rev* **57**, 397–409 (2005).
7. Tombola, F., Pathak, M. M. & Isacoff, E. Y. How does voltage open an ion channel? *Annu Rev Cell Dev Biol* **22**, 23–52 (2006).
8. Goldin, A. L. Mechanisms of sodium channel inactivation. *Curr Opin Neurobiol* **13**, 284–90 (2003).
9. Capes, D. L., Goldschen-Ohm, M. P., Arcisio-Miranda, M., Bezanilla, F. & Chanda, B. Domain IV voltage-sensor movement is both sufficient and rate limiting for fast inactivation in sodium channels. *J Gen Physiol* **142**, 101–12 (2013).
10. Kiss, T. Persistent Na-channels: origin and function. A review. *Acta Biol Hung* **59 Suppl**, 1–12 (2008).
11. Stafstrom, C. E. Persistent sodium current and its role in epilepsy. *Epilepsy Curr* **7**, 15–22 (2007).
12. Zeng, J., Powers, R. K., Newkirk, G., Yonkers, M. & Binder, M. D. Contribution of persistent sodium currents to spike-frequency adaptation in rat hypoglossal motoneurons. *J Neurophysiol* **93**, 1035–41 (2005).
13. Rybak, I. A., Ptak, K., Shevtsova, N. A. & McCrimmon, D. R. Sodium currents in neurons from the rostroventrolateral medulla of the rat. *J Neurophysiol* **90**, 1635–42 (2003).
14. Noble, D. & Noble, P. J. Late sodium current in the pathophysiology of cardiovascular disease: consequences of sodium-calcium overload. *Heart* **92 Suppl 4**, iv1–iv5 (2006).
15. Chen, S. *et al.* An increase in persistent sodium current contributes to intrinsic neuronal bursting after status epilepticus. *J Neurophysiol* **105**, 117–29 (2011).
16. Saint, D. A. The cardiac persistent sodium current: an appealing therapeutic target? *Br J Pharmacol* **153**, 1133–42 (2008).
17. Conti, C. R. Ion channel therapy of ischemic heart disease: from calcium channel blockers to late sodium current inhibition. *Clin Cardiol* **34**, 66–7 (2011).
18. Kahlig, K. M., Lepist, I., Leung, K., Rajamani, S. & George, A. L. Ranolazine selectively blocks persistent current evoked by epilepsy-associated Nanu1.1 mutations. *Br J Pharmacol* **161**, 1414–26 (2010).
19. Hodgkin, A. L. & Huxley, A. F. A quantitative description of membrane current and its application to conduction and excitation in nerve. *J Physiol* **117**, 500–44 (1952).
20. French, C. R., Sah, P., Buckett, K. J. & Gage, P. W. A voltage-dependent persistent sodium current in mammalian hippocampal neurons. *J Gen Physiol* **95**, 1139–57 (1990).
21. Stafstrom, C. E., Schwindt, P. C., Chubb, M. C. & Crill, W. E. Properties of persistent sodium conductance and calcium conductance of layer V neurons from cat sensorimotor cortex in vitro. *J Neurophysiol* **53**, 153–70 (1985).
22. Alzheimer, C., Schwindt, P. C. & Crill, W. E. Modal gating of Na+ channels as a mechanism of persistent Na+ current in pyramidal neurons from rat and cat sensorimotor cortex. *J Neurosci* **13**, 660–73 (1993).
23. Magistretti, J. & Alonso, A. Fine gating properties of channels responsible for persistent sodium current generation in entorhinal cortex neurons. *J Gen Physiol* **120**, 855–73 (2002).
24. Magistretti, J., Ragsdale, D. S. & Alonso, A. High conductance sustained single-channel activity responsible for the low-threshold persistent Na(+) current in entorhinal cortex neurons. *J Neurosci* **19**, 7334–41 (1999).
25. Magistretti, J., Ragsdale, D. S. & Alonso, A. Kinetic diversity of single-channel burst openings underlying persistent Na(+) current in entorhinal cortex neurons. *Biophys J* **85**, 3019–34 (2003).
26. Chatelier, A., Zhao, J., Bois, P. & Chahine, M. Biophysical characterisation of the persistent sodium current of the Nav1.6 neuronal sodium channel: a single-channel analysis. *Pflugers Arch* **460**, 77–86 (2010).
27. Kirsch, G. E., Skattebol, A., Possani, L. D. & Brown, A. M. Modification of Na channel gating by an alpha scorpion toxin from Tityus serrulatus. *J Gen Physiol* **93**, 67–83 (1989).
28. Richard Benzinger, G., Tonkovich, G. S. & Hanck, D. A. Augmentation of recovery from inactivation by site-3 Na channel toxins. A single-channel and whole-cell study of persistent currents. *J Gen Physiol* **113**, 333–46 (1999).
29. Jarecki, B. W., Piekarz, A. D., Jackson, J. O., 2nd. & Cummins, T. R. Human voltage-gated sodium channel mutations that cause inherited neuronal and muscle channelopathies increase resurgent sodium currents. *J Clin Invest* **120**, 369–78 (2010).
30. Rogers, M., Tang, L., Madge, D. J. & Stevens, E. B. The role of sodium channels in neuropathic pain. *Semin Cell Dev Biol* **17**, 571–81 (2006).
31. Lampert, A., Hains, B. C. & Waxman, S. G. Upregulation of persistent and ramp sodium current in dorsal horn neurons after spinal cord injury. *Exp Brain Res* **174**, 660–6 (2006).
32. Cusdin, F. S. *et al.* The sodium channel {beta}3-subunit induces multiphasic gating in NaV1.3 and affects fast inactivation via distinct intracellular regions. *J Biol Chem* **285**, 33404–12 (2010).
33. Estacion, M. & Waxman, S. G. The response of Na(V)1.3 sodium channels to ramp stimuli: multiple components and mechanisms. *J Neurophysiol* **109**, 306–14 (2013).
34. Hu, Z. *et al.* The venom of the spider Selenocosmia jiafu contains various neurotoxins acting on voltage-gated ion channels in rat dorsal root ganglion neurons. *Toxins (Basel)* **6**, 988–1001 (2014).
35. Corzo, G. *et al.* Distinct primary structures of the major peptide toxins from the venom of the spider Macrothele gigas that bind to sites 3 and 4 in the sodium channel. *FEBS Letters* **547**, 43–50 (2003).

36. Peigneur, S. *et al.* A natural point mutation changes both target selectivity and mechanism of action of sea anemone toxins. *FASEB J* **26**, 5141–51 (2012).
37. Chen, H., Gordon, D. & Heinemann, S. H. Modulation of cloned skeletal muscle sodium channels by the scorpion toxins Lqh II, Lqh III, and Lqh alphaIT. *Pflugers Arch* **439**, 423–32 (2000).
38. Lindia, J. A., Kohler, M. G., Martin, W. J. & Abbadie, C. Relationship between sodium channel NaV1.3 expression and neuropathic pain behavior in rats. *Pain* **117**, 145–53 (2005).
39. Hains, B. C. *et al.* Upregulation of sodium channel Nav1.3 and functional involvement in neuronal hyperexcitability associated with central neuropathic pain after spinal cord injury. *J Neurosci* **23**, 8881–92 (2003).
40. Cummins, T. R. *et al.* Nav1.3 sodium channels: rapid repriming and slow closed-state inactivation display quantitative differences after expression in a mammalian cell line and in spinal sensory neurons. *J Neurosci* **21**, 5952–61 (2001).
41. Catterall, W. A. *et al.* Voltage-gated ion channels and gating modifier toxins. *Toxicon* **49**, 124–41 (2007).
42. Liu, Z. *et al.* Structure and function of hainantoxin-III, a selective antagonist of neuronal tetrodotoxin-sensitive voltage-gated sodium channels isolated from the Chinese bird spider Ornithoctonus hainana. *J Biol Chem* **288**, 20392–403 (2013).
43. Kalia, J. *et al.* From Foe to Friend: Using Animal Toxins to Investigate Ion Channel Function. *J Mol Biol* (2014).
44. Baden, D. G., Bourdelais, A. J., Jacocks, H., Michelliza, S. & Naar, J. Natural and derivative brevetoxins: historical background, multiplicity, and effects. *Environ Health Perspect* **113**, 621–5 (2005).
45. Armstrong, C. M. Na channel inactivation from open and closed states. *Proc Natl Acad Sci U S A* **103**, 17991–6 (2006).
46. Cestele, S. *et al.* Structure and function of the voltage sensor of sodium channels probed by a beta-scorpion toxin. *J Biol Chem* **281**, 21332–44 (2006).
47. Cestele, S. *et al.* Voltage sensor-trapping: enhanced activation of sodium channels by beta-scorpion toxin bound to the S3–S4 loop in domain II. *Neuron* **21**, 919–31 (1998).
48. Horn, R., Ding, S. & Gruber, H. J. Immobilizing the moving parts of voltage-gated ion channels. *J Gen Physiol* **116**, 461–76 (2000).
49. Chanda, B. & Bezanilla, F. Tracking voltage-dependent conformational changes in skeletal muscle sodium channel during activation. *J Gen Physiol* **120**, 629–45 (2002).
50. Chanda, B., Asamoah, O. K. & Bezanilla, F. Coupling interactions between voltage sensors of the sodium channel as revealed by site-specific measurements. *J Gen Physiol* **123**, 217–30 (2004).
51. Campos, F. V., Chanda, B., Beirao, P. S. & Bezanilla, F. Alpha-scorpion toxin impairs a conformational change that leads to fast inactivation of muscle sodium channels. *J Gen Physiol* **132**, 251–63 (2008).
52. Wang, J. *et al.* Mapping the receptor site for alpha-scorpion toxins on a Na+ channel voltage sensor. *Proc Natl Acad Sci U S A* **108**, 15426–31 (2011).
53. Silva, J. R. & Goldstein, S. A. Voltage-sensor movements describe slow inactivation of voltage-gated sodium channels I: wild-type skeletal muscle Na(V)1.4. *J Gen Physiol* **141**, 309–21 (2013).
54. Cha, A., Ruben, P. C., George, A. L., Jr., Fujimoto, E. & Bezanilla, F. Voltage sensors in domains III and IV, but not I and II, are immobilized by Na+ channel fast inactivation. *Neuron* **22**, 73–87 (1999).
55. Groome, J. R., Dice, M. C., Fujimoto, E. & Ruben, P. C. Charge immobilization of skeletal muscle Na+ channels: role of residues in the inactivation linker. *Biophys J* **93**, 1519–33 (2007).
56. Ukomadu, C., Zhou, J., Sigworth, F. J. & Agnew, W. S. muI Na+ channels expressed transiently in human embryonic kidney cells: biochemical and biophysical properties. *Neuron* **8**, 663–76 (1992).
57. Klugbauer, N., Lacinova, L., Flockerzi, V. & Hofmann, F. Structure and functional expression of a new member of the tetrodotoxin-sensitive voltage-activated sodium channel family from human neuroendocrine cells. *EMBO J* **14**, 1084–90 (1995).
58. Lossin, C., Wang, D. W., Rhodes, T. H., Vanoye, C. G. & George, A. L., Jr. Molecular basis of an inherited epilepsy. *Neuron* **34**, 877–84 (2002).
59. Hu, H. Z. & Li, Z. W. Substance P potentiates ATP-activated currents in rat primary sensory neurons. *Brain Res* **739**, 163–8 (1996).
60. Xiao, Y. *et al.* Tarantula huwentoxin-IV inhibits neuronal sodium channels by binding to receptor site 4 and trapping the domain ii voltage sensor in the closed configuration. *J Biol Chem* **283**, 27300–13 (2008).

Acknowledgments

This work was supported by the National Basic Research Program of China (973 Program), grant no. 2010CB529801, 2012CB22305; the National Science Foundation Project, grant Nos. 31370783 and 31370817; and the Cooperative Innovation Center of Engineering and New Products for Developmental Biology of Hunan Province (grant no. 20134486).

Author contributions

C.T. and Z.L. designed experiments; C.T., X.Z., Y.Z., Z.X., Y.H., B.C., Z.H. and C.Z. performed experiments; C.T. constructed mutant and chimeric channels, C.T. and X.Z. conducted patch clamp analysis; C.T., Z.L. and S.L. contributed to manuscript preparation; C.T. and Z.L. wrote the manuscript.

Additional information

Supplementary information accompanies this paper at http://www.nature.com/scientificreports

Competing financial interests: The authors declare no competing financial interests.

How to cite this article: Tang, C. *et al.* Synergetic Action of Domain II and IV Underlies Persistent Current Generation in $Na_v1.3$ as revealed by a tarantula toxin. *Sci. Rep.* **5**, 9241; DOI:10.1038/srep09241 (2015).